Nuclear-spin effects in the photoionization of krypton

Th. A. Paul, J. Liu, and F. Merkt
Laboratorium für Physikalische Chemie, ETH Zurich, Wolfgang-Pauli-Strasse 10, 8093 Zurich, Switzerland
(Received 15 October 2008; published 6 February 2009)

The autoionizing Rydberg states of krypton close to the $^2P_{1/2}$ ionization limit were measured using a tunable narrow-bandwidth vacuum-ultraviolet laser system. The hyperfine structure of the high odd-parity autoionizing Rydberg states of ^{83}Kr was observed and analyzed. The measurements and their analysis by multichannel quantum defect theory provided information on the role of the nuclear spin in the photoionization of ^{83}Kr and on the hyperfine structure of the $^2P_{1/2}$ state of $^{83}Kr^+$. The $^2P_{1/2}$ ionization energies of all naturally occurring Kr isotopes were determined with great precision and accuracy, improving the existing literature values of the isotope-averaged ionization energy by more than one order of magnitude.

DOI: 10.1103/PhysRevA.79.022505 PACS number(s): 32.10.Fn, 32.80.Rm, 32.30.Bv

I. INTRODUCTION

The current understanding of atomic and molecular photoionization has its roots in studies of the vacuum ultraviolet (vuv) photoionization of the rare gas atoms Ne, Ar, Kr, and Xe, starting with the classic work of Beutler [1], which revealed resonances in their photoabsorption spectra beyond the first ionization threshold. These resonances are characterized by strongly asymmetric, broad profiles for the d ($l=2$) channels and almost symmetric, sharp profiles for the s ($l=0$) channels. These resonances can be assigned to Rydberg states belonging to series converging on the upper spin-orbit ($^2P_{1/2}$) component of the $(np)^5\,^2P$ ground state configuration of the rare gas ion which autoionize into the continuum associated with the lower ($^2P_{3/2}$) spin-orbit component. Fano interpreted these line shapes (now called Beutler-Fano profiles) as resulting from the interference between different ionization channels [2]. The photoionization of rare gas atoms has also served as the testing ground of multichannel quantum defect theory (MQDT) [3–8] which today represents the theory best suited to describe the photoionization dynamics of atoms and molecules near low-lying thresholds [9–11].

The electronic spectrum of krypton has been studied extensively, and the positions of many bound and autoionizing levels have been compiled in tables [12–14]. The autoionizing states have been accessed from the $^1S_0$ ground state by vuv excitation using vacuum spectrographs. The first absorption spectrum of the s and d autoionizing states of krypton was measured by Beutler [1]. Yoshino and Tanaka reported the first accurate value of the second ionization energy of krypton [118 284.6(2) cm^{-1}] [15]. Wu *et al.* [16], Ueda *et al.* [17], and Maeda *et al.* [18,19] later determined the vuv absorption cross sections and presented line shape analyses of the autoionizing resonances. The odd-parity autoionizing states can also be accessed using multiphoton excitation schemes or by single-photon excitation in the visible or ir range from metastable atoms ($^3P_{2,0}$) produced in discharges. Three-photon excitation of the odd-parity states of Kr was reported by Dehmer and Dehmer [20] and Koeckhoven *et al.* [21], and two-photon excitation from metastable levels by Ahmed *et al.* [22] and Klar *et al.* [23], who also presented a MQDT analysis of the spectra. The autoionizing resonance profiles of the noble gases were also studied experimentally and theoretically by Klar *et al.* [24], Petrov *et al.* [25], and Peters *et al.* [26]. Investigations of the Stark effect in autoionizing states of Kr were performed by Delsart *et al.* [27] using two-step laser excitation from a metastable state and by Kampschulte *et al.* [28] by fluorescence dip spectroscopy. Optogalvanic spectra of the $(n+2)s'$ and nd' autoionizing states were reported by Wada and Hirose [29] and recently by Baig and Aslam [30].

Limitations imposed by either insufficient experimental resolution or the inability to record spectra of selected isotopes have so far prevented both the recording of spectra of the autoionizing Rydberg states at principal quantum number beyond $n=60$ [15] and the obtaining of isotope-specific spectroscopic data. No studies of the hyperfine structure of the autoionizing resonances of ^{83}Kr have been described in the literature. Experimental data on the hyperfine structure of autoionizing Rydberg states are exceptionally scarce and have only been obtained on the spin-orbit autoionizing levels of atomic Xe [31] and the rotationally autoionizing levels of ortho-H_2 [32]. The present study of the hyperfine structure of the autoionizing Rydberg states of Kr thus represents the third study of the role of nuclear spins in photoionization.

The photoionization of Kr leads to the formation of an open-shell $(4p)^5\,^2P_{J^+}$ Kr^+ cation with a large spin-orbit splitting (approximately 5370 cm^{-1}). In the case of $^{83}Kr^+$, each spin-orbit level is split further by the hyperfine interaction. The energy-level structures of the $I=0$ isotopes of Kr^+ and $^{83}Kr^+$ are compared in Fig. 1, which also schematically depicts the ionization channels and autoionization processes. The main scientific motivations for the investigation of the autoionizing resonances of Kr by high-resolution spectroscopy presented in this paper were (1) to measure the hyperfine structure of the autoionizing Rydberg states of ^{83}Kr and to quantify the role of the $I=9/2$ nuclear spin in the photoionization dynamics, (2) to determine accurate ionization energies of all isotopes of krypton, (3) to obtain, by extrapolation of the autoionizing Rydberg series, the hyperfine structure of the $^2P_{1/2}$ spin-orbit excited state of $^{83}Kr^+$, (4) to assess the ability of MQDT to reproduce the observed spectral structures, and (5) to use MQDT to predict the spectral structures and photoionization dynamics that are linked to the transfer of hyperfine energy from the ion to the Rydberg electron in the process of autoionization.

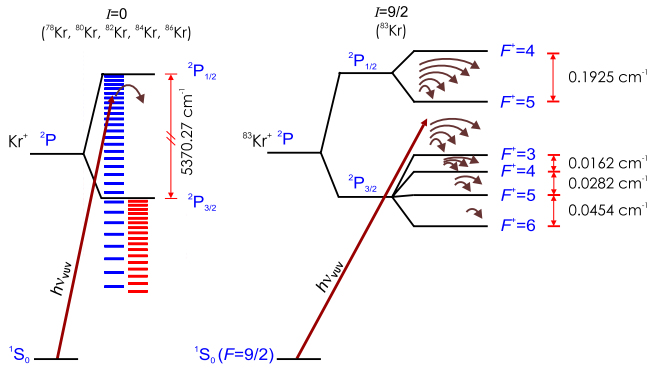

FIG. 1. (Color online) Schematic energy-level diagram of the autoionizing Rydberg states of Kr. The ^2P electronic ground state of Kr^+ splits into two spin-orbit components, separated by $\sim 5370\ cm^{-1}$. Rydberg states converging to the upper, $^2P_{1/2}$, spin-orbit state of the ion can undergo autoionization into the continua of channels associated with the ion core in the $^2P_{3/2}$ spin-orbit state. In the case of ^{83}Kr ($I=9/2$), both the lower and the upper spin-orbit components are split further into hyperfine components designated by the quantum number F^+, which indicates the total angular momentum of the ion including nuclear spin. The arrows indicate the autoionization processes that are in principle allowed. The Rydberg states converging on the $F^+=3-5$ hyperfine components of the $^2P_{3/2}$ state located above the position of the $F^+=6$ hyperfine component can only decay by hyperfine autoionization.

II. EXPERIMENT

A. Experimental setup

The vacuum ultraviolet radiation around 84 nm, required to access the autoionizing region between the $^2P_{3/2}$ and $^2P_{1/2}$ ionization thresholds of Kr, was generated by two-photon resonance-enhanced sum-frequency mixing ($\tilde{\nu}_{vuv}=2\tilde{\nu}_1+\tilde{\nu}_2$) in a Kr gas jet from the outputs of a titanium:sapphire laser system described in detail in Refs. [33,34]. Briefly, the laser system consists of two near-infrared (nir) continuous-wave (cw) Ti:sapphire ring lasers from which nir pulses of freely adjustable duration ($\sim$40 ns for this experiment) are obtained by use of acousto-optic modulators. After pulse amplification in neodymium-doped yttrium aluminum garnet–(Nd:YAG)-pumped Ti:sapphire crystals, uv radiation at wave numbers $\tilde{\nu}_1$ and $\tilde{\nu}_2$ is produced from the intense nir pulses using nonlinear crystals. For the present measurements, the wave number $\tilde{\nu}_1$ of the first laser was locked at the position $2\tilde{\nu}_1 \approx 94\,092.87\ cm^{-1}$ of the $(4P)^5 5p[1/2]_0 \leftarrow {}^1S_0$ two-photon transition in krypton [35], while the wave number $\tilde{\nu}_2$ of the second laser remained tunable. The fixed-frequency ultraviolet (uv) laser beam at $2\tilde{\nu}_1=94\,092.87\ cm^{-1}$ was obtained by frequency quadrupling the amplified nir output ($\sim$15 mJ) of the Ti:sapphire laser system using two β–barium borate (BBO) crystals. Frequency doubling in BBO of the amplified nir output of the tunable laser ($\sim$10 mJ) delivered the uv laser beam in the range $\tilde{\nu}_2=24\,120-24\,192\ cm^{-1}$ required for sum-frequency generation in the desired vuv wave-number range. The vuv beam intersected, at right angles, a skimmed supersonic expansion of Kr gas (purity 4.0, 3 bar nozzle stagnation pressure). A skimmer with an orifice diameter of 0.5 mm was placed 26 cm upstream from the point of intersection. Excitation of Kr atoms occurred at the center of a cylindrically symmetric stack of eight graphite-coated electrodes used for applying pulsed electric fields and for compensating stray electric fields. Kr^+ ions produced by photoionization were extracted by a pulsed electric field of 460 V/cm applied 3 μs after photoexcitation and were detected by a microchannel plate detector located at the end of a 30-cm-long flight tube. Isotope-selective detection was achieved by setting integrator gates on the time-of-flight mass spectra. In order to reduce perturbing effects on the Rydberg atoms of polar molecules in the background gas (mostly H_2O), the pressure in the photoexcitation chamber was held below 5×10^{-10} mbar. Spectra of the autoionizing Rydberg states of the isotopes of Kr were recorded by monitoring the corresponding Kr^+ ion signals as a function of the wave number $\tilde{\nu}_2$ of the second laser.

Part of the nir cw output of the tunable ring laser was used for scan linearization and calibration: This was achieved by recording, simultaneously with the Kr^+ ion signal, the transmission spectra through a temperature-stabilized Vernier étalon of free spectral range (FSR) 6.7587 GHz and a passively stabilized confocal étalon of FSR 161.36 MHz. Monitoring the nir absorption signal of a 1-m-long iodine vapor cell heated to 600 °C allowed the absolute frequency of the nir radiation to be determined using the iodine atlas [36].

Frequency stabilization of the fixed-frequency laser to 1/8 of the frequency position of the two-photon resonance in the nonlinear gas was accomplished by locking laser 1 to a transmission maximum of a He-Ne stabilized confocal Fabry-Pérot cavity with a FSR of 150.08 MHz and a finesse of 30, through which part of the cw nir output was directed. The locking procedure, which needed to be performed only once a day, involved scanning the laser while recording both the Fabry-Pérot cavity transmission signal and the absorption signal of an iodine vapor cell (heated to 600 °C, absorption path length 2 m). The absolute frequency position of every transmission maximum of the Fabry-Pérot cavity, and thus that of the locked ring laser, was determined by comparison of the recorded I_2 spectrum with a reference Doppler-free I_2 absorption spectrum calibrated using a femtosecond frequency comb [37].

B. Error budget

The vuv wave number was determined by building the sum

$$\tilde{\nu}_{vuv} = 8(\tilde{\nu}_{nir,1} + \Delta\tilde{\nu}^{AOM}_{nir,1} + \Delta\tilde{\nu}_{amp}) + 2(\tilde{\nu}_{nir,2} + \Delta\tilde{\nu}^{AOM}_{nir,2} + \Delta\tilde{\nu}_{amp}) + \Delta\tilde{\nu}_{Doppler}, \quad (1)$$

where $\tilde{\nu}_{nir,1}$ and $\tilde{\nu}_{nir,2}$ are the wave numbers of the cw outputs of the fixed-frequency and tunable Ti:sapphire ring lasers, respectively. $\Delta\tilde{\nu}_{amp}$ stands for the wave-number shift arising in the Ti:sapphire amplifier, and $\Delta\tilde{\nu}^{AOM}_{nir,i}$ ($i=1,2$) represent the wave-number shifts of the first-order sideband of the acousto-optic modulator (AOM) outputs corresponding to +1 GHz. $\Delta\tilde{\nu}_{Doppler}$ represents the Doppler shift which arises from a possible deviation of the angle between the vuv beam and the probe gas jet from 90°.

TABLE I. Sources of relative uncertainty contributing to the overall measurement uncertainties.

Source of relative uncertainty	Uncertainty (MHz)
Line maximum determination (s' lines)	2×10
Scan linearization	2×3
I_2 calibration (tunable laser)	2×30
Stability of lock position	8×2.5
Total relative uncertainty	66

The uncertainties in the spectral positions presented here can be classified into those affecting only the relative positions (hereafter called relative uncertainties) and those affecting only the absolute positions (absolute uncertainties). The error budget is summarized in Tables I and II, respectively.

Relative uncertainties that arise from the determination of the line centers (relevant for the sharp $s'[1/2]_1$ lines) correspond to twice the step size of 10 MHz of the nir frequency (because of frequency doubling). The relative uncertainty associated with the scan linearization was derived from the comparison of the experimental étalon frequency marker traces with calculated Airy functions. The relative uncertainty related to the iodine calibration procedure was determined by comparing the measured intervals between I_2 lines with the corresponding intervals in the iodine atlas [36]. The relative uncertainty in the lock position of laser 1 corresponds to the half-width (2.5 MHz) of the transmission maxima of the He-Ne-stabilized Fabry-Pérot cavity.

Contributions to the absolute uncertainty include the uncertainty in the Doppler shift, which was determined from a comparison of measurements of individual sharp transitions in supersonic expansions of neat Kr, a 1:9 Kr:Xe gas mixture, and a 1:6 Kr:Ar gas mixture. The analysis of the Doppler shifts resulting from the different beam velocities was made using Eq. (1) of Ref. [38]. The frequency shift $\Delta\nu_{\mathrm{amp}}$ occurring in the Ti:sapphire amplifier was measured in a heterodyne beat experiment in which the amplified beam was spatially overlapped with a cw reference beam shifted by −1 GHz from the frequency of the unamplified beam. The measurement confirmed the value of the frequency shift of $\Delta\nu_{\mathrm{amp}}=-5\pm2$ MHz observed previously [33], and did not reveal any frequency evolution (frequency chirp) during the pulses. The uncertainty in the absolute lock position of laser 1, 30 MHz in the nir, was limited by the comparison between the recorded Doppler-broadened I_2 absorption feature in the vicinity of the locking point with a Doppler-free iodine absorption reference spectrum [37]. For the comparison, the Doppler-free spectrum was convoluted with a Gaussian profile of full width at half maximum equal to the Doppler width expected at the temperature of the iodine vapor cell ($0.02\ \mathrm{cm}^{-1}$).

TABLE II. Sources of absolute uncertainty contributing to the overall measurement uncertainties.

Source of absolute uncertainty	Uncertainty (MHz)
Doppler shift	65
Frequency shift in the Ti:sapphire amplifier	10×2
I_2 calibration (tunable laser)	2×150
Absolute lock position	8×30
ac Stark shift	$\leqslant20$
Pressure shift	$\leqslant20$
Total absolute uncertainty	390

The uncertainty of 500 kHz in the absolute position of the $a1$ hyperfine component of the I_2 transition $R(107)(20\text{-}1)$ at $11\,761.616\,17\ \mathrm{cm}^{-1}$ in the reference spectrum is negligible. The absolute uncertainty resulting from the accuracy of the transition wave numbers in the Doppler-broadened I_2 atlas [36] affects only the determination of the wave number of the tunable laser. ac Stark shifts and pressure shifts were found to be negligible in experiments in which the laser power and the stagnation pressure of the probe gas nozzle were varied.

III. MQDT TREATMENT OF THE AUTOIONIZING STATES OF KRYPTON

The Rydberg states of the rare gas atoms are usually labeled in Racah-type notation as $nl^{(\prime)}[K]_J$, where the prime after the value of the orbital angular momentum quantum number l designates Rydberg levels belonging to series converging on the upper ($^2P_{1/2}$) spin-orbit component of Kr^+. K is the quantum number associated with the angular momentum vector $\vec{K}$, and J represents the total angular momentum quantum number excluding nuclear spin. The angular momentum coupling scheme can be described as follows:

$$\vec{L}^+ + \vec{S}^+ = \vec{J}^+,$$

$$\vec{J}^+ + \vec{l} = \vec{K},$$

$$\vec{K} + \vec{s} = \vec{J},$$

where L^+ and S^+ are the orbital and electron spin angular momentum quantum numbers of the ionic state, and l and s the corresponding quantum numbers of the Rydberg electron, respectively. This coupling scheme is intermediate between the more familiar LS and jj coupling schemes.

The treatment of Rydberg spectra by MQDT relies on separating the ion-core-Rydberg-electron system into a close-coupling and a long-range spatial region and modeling the interaction of the Rydberg electron with the ion core as a collision. This approach is successful in describing the bound, autoionizing, and continuum regions of atomic and molecular spectra [3,5–7,39].

The analysis by MQDT of the photoionization spectra of the isotopes of Kr relied on parameters derived in earlier MQDT analyses of the absorption spectrum of Kr by Aymar *et al.* [40] (not isotope selective), of the pulsed-field-ionization spectrum of ^{83}Kr below the ($^2P_{3/2}$) threshold [41], and of very high-resolution millimeter-wave spectra [42], which enabled the derivation of an almost complete set of accurate quantum defect parameters μ_α and $V_{\alpha\alpha'}$, including

TABLE III. The 16 s and d ionization channels of the $I=0$ isotopes of Kr designated in LS coupling. The values of F in the case of ^{83}Kr are given in parentheses. There are 72 channels in ^{83}Kr, 44 of which ($F=7/2,9/2,11/2$) are optically accessible from the $^1S_0$ ($F=9/2$) ground state.

	$J=0$ ($F=9/2$)	$J=1$ ($F=7/2-11/2$)	$J=2$ ($F=5/2-13/2$)	$J=3$ ($F=3/2-15/2$)	$J=4$ ($F=1/2-17/2$)
s	$^3P_0$	$^1P_1$	$^3P_2$		
		$^3P_1$			
d	$^3P_0$	$^1P_1$	$^3P_2$	$^3D_3$	$^3F_4$
		$^3P_1$	$^1D_2$	$^1F_3$	
		$^3D_1$	$^3D_2$	$^3F_3$	
			$^3F_2$		

their first-order energy dependence. The present analysis followed closely that of the autoionizing Rydberg states of Xe presented by Wörner *et al.* [31].

In the close-coupling region, the Rydberg electron is strongly coupled to the ion core through electrostatic (including exchange) interactions with the core electrons. In this region, the ion-core-Rydberg-electron system can be approximately, though not perfectly (see below), described by LS coupling:

$$\vec{L}^+ + \vec{l} = \vec{L},$$

$$\vec{S}^+ + \vec{s} = \vec{S},$$

$$\vec{L} + \vec{S} = \vec{J}.$$

In the case of the odd-parity s and d Rydberg states of Kr, 16 LS-coupled channels need to be considered (see Table III). Each channel α can be described in first approximation by eigenquantum defects μ_α which are proportional to the phase shifts $\mu_\alpha \pi$ experienced by the electron wave function in the core region. Because the hyperfine interaction is negligible compared to the Coulomb and exchange interactions in the close-coupling region, it makes no contribution to the collisional phase shifts and thus to the quantum defects. Consequently, the treatment of the hyperfine structure of ^{83}Kr ($I=9/2$) and the other isotopes relies on the same MQDT parameters, as explained in Ref. [41].

In the long-range region of the ion-core–Rydberg-electron collision, the interaction potential is a simple $-1/r$ Coulomb potential (in atomic units). The channels, so-called dissociation channels i, are best described by the direct products of the ion-core wave function and the Rydberg-electron wave function. J^+j coupling,

$$\vec{L}^+ + \vec{S}^+ = \vec{J}^+,$$

$$\vec{l} + \vec{s} = \vec{j},$$

$$\vec{J}^+ + \vec{j} = \vec{J},$$

is adequate to describe the angular momentum coupling hierarchy in this region. The long-range ionization channels corresponding to the odd-parity s and d Rydberg states of Kr are listed in Table IV.

In the MQDT treatment, the Rydberg-electron wave function is forced to be continuous at the boundary between the close-coupling and the long-range regions. For the angular part of the wave function, this is achieved by an angular momentum frame transformation $U_{i\alpha}=\langle \alpha | i \rangle$ between the close-coupling channels α and the dissociation channels i. The elements of $U_{i\alpha}$ are factorized

$$U_{i\alpha} = \sum_{\alpha'} U_{i\alpha'} V_{\alpha\alpha'}, \tag{2}$$

where

TABLE IV. The 16 s and d ionization channels of the $I=0$ isotopes of Kr designated in J^+j coupling. The last column gives the 72 corresponding channels of ^{83}Kr. Only the $F=7/2$, $9/2$, and $11/2$ channels, i.e., 44 channels, are optically accessible from the $^1S_0$ ($F=9/2$) ground state.

J^+	j	J	F
$1/2$	$s(j=1/2)$	0; 1	$9/2$; $7/2-11/2$
	$d(j=3/2)$	1; 2	$7/2-11/2$; $5/2-13/2$
	$d(j=5/2)$	2; 3	$5/2-13/2$; $3/2-15/2$
$3/2$	$s(j=1/2)$	1; 2	$7/2-11/2$; $5/2-13/2$
	$d(j=3/2)$	0; 1; 2; 3	$9/2$; $7/2-11/2$; $5/2-13/2$; $3/2-15/2$
	$d(j=5/2)$	1; 2; 3; 4	$7/2-11/2$; $5/2-13/2$; $3/2-15/2$; $1/2-17/2$

$$U_{i\alpha'} = \langle LSJ|J^+jJ\rangle = \sqrt{(2J^+ + 1)(2j + 1)(2L + 1)(2S + 1)} \times \begin{Bmatrix} L^+ & S^+ & J^+ \\ l & s & j \\ L & S & J \end{Bmatrix} \tag{3}$$

is the analytical frame transformation matrix between the LS-coupled and the J^+j-coupled basis, and $V_{\alpha\alpha'}$ accounts for the departure from ideal LS coupling of the close-coupling channels. In Eq. (3), the quantity in the large parentheses is a $9j$ symbol [43]. The positions of the bound levels are described by the parametrized effective quantum number

$$\nu_i = \sqrt{\frac{R_M}{E_{i,J^+} - \tilde{\nu}}}, \tag{4}$$

where R_M is the mass-dependent Rydberg constant, E_{i,J^+} is the energetic position of the $^2P_{J^+}$ ionic state above the $^1S_0$ neutral ground state, and $\tilde{\nu}$ represents the total energy of the system. In the discrete part of the spectrum, located below the first ionization threshold, all channels are closed and the wave functions must vanish at infinite distance from the nucleus. This boundary condition is satisfied when [6]

$$\sum_\alpha U_{i\alpha} \sin[\pi(\mu_\alpha + \nu_i)]A_\alpha = 0. \tag{5}$$

In Eq. (5), A_α is the expansion coefficient of the radial part of the Rydberg-electron wave function in the basis of the close-coupling eigenchannels. In the spectral region between the two ionization thresholds, the boundary condition for the dissociation channels which remain closed ($i \in Q$) is still described by Eq. (5). The dissociation channels that are open behave as collision eigenchannels, ρ, undergoing a phase shift τ_ρ. The modified boundary condition for the open dissociation channels ($i \in P$) can be expressed as [6]

$$\sum_\alpha U_{i\alpha} \sin[\pi(-\tau_\rho + \mu_\alpha)]A_\alpha = 0. \tag{6}$$

The solutions that simultaneously satisfy Eqs. (5) and (6) are obtained by solving a generalized eigenvalue problem [10],

$$\mathbf{\Gamma A}^\rho = \tan(\pi\tau_\rho)\mathbf{\Lambda A}^\rho. \tag{7}$$

At each energy in the autoionization region, Eq. (7) has as many solutions (τ_ρ and expansion coefficients $\mathbf{A}^\rho$) as there are open channels. In Eq. (7),

$$\Gamma_{i\alpha} = \begin{cases} U_{i\alpha} \sin[\pi(\nu_i + \mu_\alpha)] & \text{for } i \in Q, \\ U_{i\alpha} \sin(\pi\mu_\alpha) & \text{for } i \in P, \end{cases} \tag{8}$$

and

$$\Lambda_{i\alpha} = \begin{cases} 0 & \text{for } i \in Q, \\ U_{i\alpha} \cos(\pi\mu_\alpha) & \text{for } i \in P. \end{cases} \tag{9}$$

Implementation of nuclear spin is achieved by increasing the number of eigenchannels that are required for a description of the s and d channels from 16 to 44, where the LS and J^+j coupling schemes are extended to include nuclear spin, i.e., for LS coupling, $\vec{J}+\vec{I}=\vec{F}$ and for J^+j coupling $\vec{J}^+ + \vec{I} = \vec{F}^+$ (see Tables III and IV). The analytical frame-transformation matrix is then [41]

$$\begin{aligned} U_{i\alpha'} = \langle LSJF|J^+F^+jF\rangle = (2F + 1)\sqrt{(2J + 1)(2L + 1)(2S + 1)(2j + 1)(2F^+ + 1)(2J^+ + 1)} \\ \times \sum_{m_j,m_{J^+},m_J,m_l,m_{L^+},m_L,m_s,m_{S^+},m_S,m_{F^+},m_I} (-1)^{F^+ - j - J^+ + 2I - J + L - S - 2s + 3m_F + m_{J^+} + 2m_J} \\ \times \begin{pmatrix} I & J & F \\ m_I & m_J & -m_F \end{pmatrix} \begin{pmatrix} L & S & J \\ m_L & m_S & -m_J \end{pmatrix} \begin{pmatrix} L^+ & l & L \\ m_{L^+} & m_l & -m_L \end{pmatrix} \begin{pmatrix} S^+ & s & S \\ m_{S^+} & m_s & -m_S \end{pmatrix} \begin{pmatrix} F^+ & j & F \\ m_{F^+} & m_j & -m_F \end{pmatrix} \\ \times \begin{pmatrix} l & s & j \\ m_l & m_s & -m_j \end{pmatrix} \begin{pmatrix} I & J^+ & F^+ \\ m_I & m_{J^+} & -m_{F^+} \end{pmatrix} \begin{pmatrix} L^+ & S^+ & J^+ \\ m_{L^+} & m_{S^+} & -m_{J^+} \end{pmatrix}. \end{aligned} \tag{10}$$

The close-coupling quantum defects μ_α are the same as for the $I=0$ isotopes, as explained above. The main difference in the treatment of ^{83}Kr compared to the treatment of the $I=0$ isotopes, next to the fact that many more ionization channels must be defined, is that the parametrized effective principal quantum number $\nu_i = \nu_{J^+F^+}$ must be determined with respect to the positions of the $F^+=4$ and $F^+=5$ components of the $J^+=1/2$ upper spin-orbit component of $^{83}Kr^+$, E_{i,J^+F^+}. The positions of these levels were not precisely known at the outset of this investigation and they had to be optimized in the course of the MQDT analysis of the spectra.

The intensity distribution of the spectra is determined by the transition dipole amplitude D_α for transitions to the close-coupling channels [6,41]. In the case of single-photon excitation of the odd-parity s and d Rydberg states of Kr from the $^1S_0$ ground state, D_α is zero for all channels with $J \neq 1$ and/or $S=1$, so that only two dipole amplitudes for the $ns\ ^1P_1$ and $nd\ ^1P_1$ channels are necessary. From the dipole amplitudes D_α, reduced dipole matrix elements $D(i,F)$ can be determined from summation of the contributions of the collision eigenfunctions ρ of the open dissociation channels (see [31] for further discussion):

$$D(i,F) = \sum_{\rho} e^{i(\sigma_i - \pi l_i/2)} \langle i|\rho\rangle e^{i\pi\tau_\rho} \sum_{\alpha} \frac{A_\alpha^\rho D_\alpha}{N_\rho}, \tag{11}$$

where the label F is used only for $I \neq 0$ isotopes. In Eq. (11),

$$\sigma_i = \mathrm{Arg}\left[\Gamma\left(l_i + 1 - i\sqrt{\frac{R_M}{E_{i,J^+F^+} - \tilde{\nu}}}\right)\right], \tag{12}$$

$$\langle i|\rho\rangle = \frac{\sum_{\alpha} U_{i\alpha} \cos[\pi(-\tau_\rho + \mu_\alpha)] A_\alpha^\rho}{N_\rho}, \tag{13}$$

and

$$N_\rho^2 = \sum_{i \in P} \left(\sum_{\alpha} U_{i\alpha} \cos[\pi(-\tau_\rho + \mu_\alpha)] A_\alpha^\rho\right)^2. \tag{14}$$

The partial photoionization cross section σ_i in the ionization continuum of channel i, labeled by the quantum number J^+ for the $I=0$ isotopes and J^+F^+ for the $I \neq 0$ isotope, is then given by [44]

$$\sigma_{J^+F^+} \propto \omega \sum_F W_F \sum_{i \in P_{J^+F^+}} |D(i,F)|^2, \tag{15}$$

where ω represents the frequency of the ionizing radiation and $W_F = (2F+1)/(2I+1)$ accounts for the multiplicity of the levels accessed by photoionization from the $^1S_0$ ground state [45] and is relevant only for $I \neq 0$ isotopes.

The total photoionization cross section is then obtained as [31]

$$\sigma_{\mathrm{tot}} = \sum_{J^+F^+} \sigma_{J^+F^+}. \tag{16}$$

σ_{tot} corresponds to the intensity measured in the photoionization spectra. The partial photoionization cross section $\sigma_{J^+F^+}$ can be used to predict branching ratios for photoionization into different spin-orbit and hyperfine dissociation channels.

IV. RESULTS

A. Photoionization spectra of the $I=0$ isotopes of Kr

The spectrum of the s' and d' $J=1$ autoionizing Rydberg states of Kr consists of successive pairs of resonances: broad blue-degraded resonances corresponding to transitions to the $nd'[3/2]_1$ Rydberg states and sharp resonances corresponding to a transitions to the $ns'[1/2]_1$ Rydberg states. These resonances have been the object of numerous studies (see Sec. I). The s' and d' autoionizing resonances display the characteristic Beutler-Fano profiles [2,46] described by [47,48]

$$\sigma_{\mathrm{tot}} = \sigma_{\mathrm{as}} \frac{(\epsilon_{\mathrm{s}} + q_{\mathrm{s}})^2}{1 + \epsilon_{\mathrm{s}}^2} + \sigma_{\mathrm{ad}} \frac{(\epsilon_{\mathrm{d}} + q_{\mathrm{d}})^2}{1 + \epsilon_{\mathrm{d}}^2} + \sigma_{\mathrm{b}}. \tag{17}$$

In Eq. (17), σ_{tot} is the total photoabsorption cross section, σ_{as} and σ_{ad} are the photoabsorption cross sections associated with open channels that can interact with the s' and d' discrete states, respectively, and σ_{b} is the nonresonant contribution to the total photoabsorption cross section. q_l is the asymmetry parameter and ϵ_l represents a periodic energy scale adapted to the regular structure of the Rydberg series:

$$\epsilon_l = \tan[\pi(\nu_{1/2} + \mu_l)]/W_l. \tag{18}$$

In Eq. (18), W_l denotes the width parameter which is related to the autoionization rate Γ_{nl} by

$$\Gamma_{nl} = \frac{4R_M W_l}{\pi(n - \mu_l)^3} = \frac{\Gamma_{nl}^*}{(n^*)^3}, \tag{19}$$

where μ_l is the quantum defect and $\nu_{1/2}$ is the parametrized effective principal quantum number with respect to the $J^+ = 1/2$ ionization threshold. To a good approximation the re-

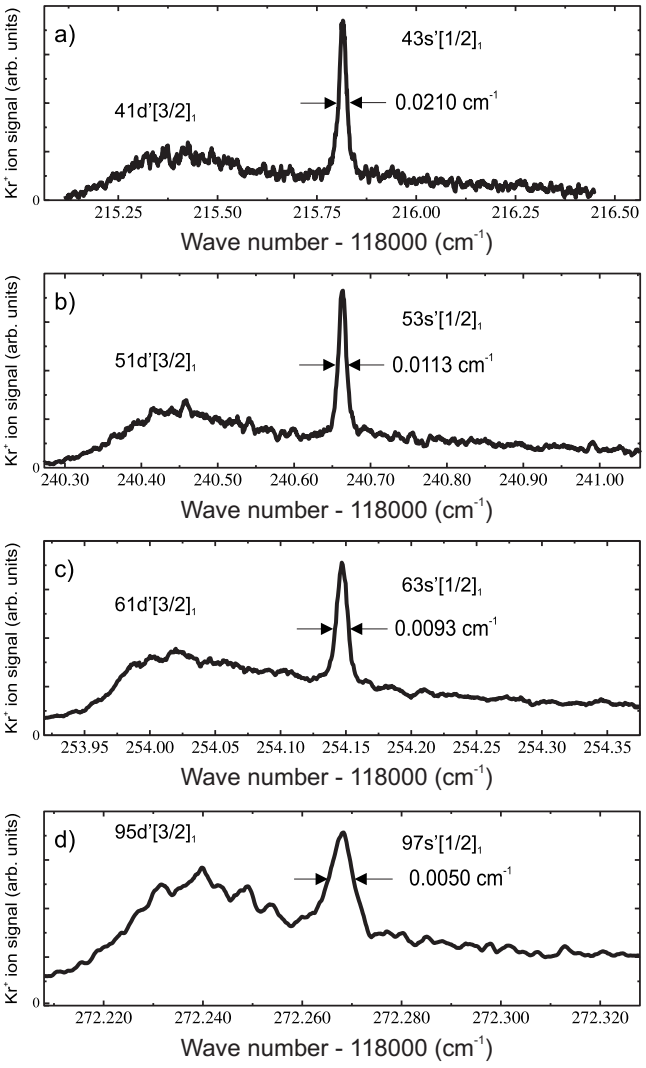

FIG. 2. Spectra of the $(n+2)s'[1/2]_1$ and $nd'[3/2]_1$ Rydberg states of ^{84}Kr observed for $n=41$, 51, 61, and 95 in (a), (b), (c), and (d), respectively (see text for details). The horizontal scale of each panel has been chosen so that the resonance profiles can be compared directly. The measured widths of the s' and d' resonances decrease as $1/n^3$ until the natural width becomes comparable to or smaller than the experimental bandwidth. This is the case for the s' resonance at $(n+2)=97$ (d).

TABLE V. Wave numbers of the $4p^5(n+2)s'[1/2]_1 \leftarrow {}^1S_0$ and $4p^5nd'[1/2]_1 \leftarrow {}^1S_0$ transitions of $I=0$ isotopes of Kr. The relative and absolute uncertainties in the line positions correspond to 0.002 and 0.013 cm^{-1}, respectively.

$(n+2)s'$	$\tilde{\nu}(^{80}Kr)$ (cm^{-1})	$\tilde{\nu}(^{82}Kr)$ (cm^{-1})	$\tilde{\nu}(^{84}Kr)$ (cm^{-1})	$\tilde{\nu}(^{86}Kr)$ (cm^{-1})	nd'	$\tilde{\nu}(^{84}Kr)$ (cm^{-1})
43	118215.7992	118215.8050	118215.8138	118215.8220	41	118215.2942
48	118230.2765	118230.2827		118230.2988		
53	118240.6472	118240.6547	118240.6630	118240.6711	51	118240.4042
63	118254.1302	118254.1386	118254.1470	118254.1547	61	118253.9997
64	118255.1238	118255.1324	118255.1410	118255.1491	62	118254.9982
75	118263.4811	118263.4892	118263.4981	118263.5054	73	118263.4174
84	118267.9385	118267.9483	118267.9574	118267.9642		
85		118268.3648	118268.3705			
86		118268.7465	118268.7542	118268.7621		
87	118269.1135	118269.1229	118269.1323	118269.1393		
88		118269.4882	118269.4961	118269.5036		
89	118269.8320	118269.8409	118269.8472	118269.8564		
90	118270.1624		118270.1813	118270.1911		
91	118270.4998	118270.5092	118270.5176	118270.5244		
92	118270.8150	118270.8247	118270.8344	118270.8420		
93	118271.1215	118271.1313	118271.1403	118271.1491		
94	118271.4206	118271.4290	118271.4367	118271.4441		
95	118271.7064	118271.7147	118271.7251	118271.7317	93	118271.6961
96	118271.9862	118271.9939	118272.0015	118272.0100		
97	118272.2520	118272.2581	118272.2682	118272.2763		
98	118272.5138	118272.5196	118272.5290	118272.5372		
99		118272.7720	118272.7820	118272.7898		
100	118273.0095	118273.0167	118273.0251	118273.0340		
101		118273.2542	118273.2623	118273.2708		
102	118273.4765	118273.4844	118273.4937	118273.5012		
103	118273.7006	118273.7081	118273.7167	118273.7249		
104	118273.9188	118273.9250	118273.9339	118273.9411		
105		118274.1323	118274.1409	118274.1472		
106		118274.3360	118274.3451	118274.3516		
107		118274.5335	118274.5443	118274.5506		
116			118276.1076	118276.1140		
117		118276.2490	118276.2569	118276.2643		
118		118276.3948	118276.4031			
119			118276.5459			
120			118276.6853	118276.6922		
121		118276.8117		118276.8285		
122		118276.9426	118276.9526			
123		118277.0747	118277.0817			
124		118277.1988				
125			118277.3291	118277.3361		
126			118277.4466	118277.4569		
127		118277.5553	118277.5647	118277.5746		
128		118277.6692				
129		118277.7800				
130			118277.8991			
131			118278.0047			

TABLE VI. Ionization energies of the isotopes of Kr. The value of $E_{i,J^+=1/2}$ for ^{83}Kr corresponds to the position of the barycenter of the $F^+=5$ and $F^+=4$ hyperfine states of $^{83}Kr^+$ ($^2P_{1/2}$) determined in a MQDT forward calculation; see Sec. IV B.

Isotope	Natural abundance (%)	Ionization energy $E_{i,J^+=1/2}$ (cm^{-1})	Statistical uncertainty (cm^{-1})	Absolute uncertainty (cm^{-1})	Isotope shift (cm^{-1})
^{78}Kr	0.35(1)	118284.6813[a]	0.0020	0.019	−0.03216(72)[a]
^{80}Kr	2.28(1)	118284.6903	0.0027	0.019	−0.02396(75)[a]
^{82}Kr	11.58(14)	118284.6951	0.0017	0.019	−0.01648(63)[b]
^{83}Kr	11.49(6)	118284.6965	0.0032	0.019	
^{84}Kr	57.00(4)	118284.7045	0.0017	0.019	−0.00763(57)[b]
^{86}Kr	17.30(22)	118284.7135	0.0019	0.019	0

[a]Obtained from the linear dependence of the isotope shifts of the measured $I=0$ isotopes of 0.004 02(9) cm^{-1} per mass unit.
[b]Obtained from the averaged isotope shifts of $(n+2)s'[1/2]_1$ Rdberg states in the region $n=41-102$.

duced width Γ^*_{nl} is independent of $n^*=n-\mu_l$ and characteristic of a series with given K and J.

In the present study, the photoionization spectrum of Kr was recorded between 118 210 and 118 285 cm^{-1} and contains information on the autoionization resonances from $n=41$ to the $^2P_{1/2}$ ionization threshold. Figure 2 shows four pairs of s' and d' resonances of ^{84}Kr at $n=41$ (a), 51 (b), 61 (c), and 95 (d). The widths of the s' resonances decrease from 0.0210 cm^{-1} at $(n+2)=43$ to 0.0050 cm^{-1} at $(n+2)=97$. They follow the n^{-3} scaling law [Eq. (19)] closely up to $n\approx 90$, at which point Doppler broadening and the vuv laser bandwidth start making important contributions to the measured widths of the resonances.

The long progressions of resonances recorded for the isotopes ^{80}Kr, ^{82}Kr, ^{84}Kr, and ^{86}Kr, the positions of which are given in Table V, allowed the determination of their ionization energies using two methods: The first consisted of fitting the spectra in the region $n=41-82$ with Eq. (17), and also led to the determination of the parameters μ_l, q_l, and Γ^*_{nl}. The second method allowed inclusion of the higher-n states, employing a least-squares fitting routine based on the Rydberg formula. The values of μ_l and $E_{i,J^+=1/2}$ obtained by both procedures agreed within their uncertainties. The ionization energies of the natural isotopes of Kr are listed in Table VI with their statistical and absolute uncertainties, as well as the isotope shifts relative to $E_{i,J^+=1/2}(^{86}\mathrm{Kr})$. The values of $E_{i,J^+=1/2}$ of the different $I=0$ isotopes were obtained by taking the weighted averages of the results of the two extraction procedures. The ionization energy of ^{83}Kr corresponds to the barycenter of the two hyperfine states of the spin-orbit excited $^{83}Kr^+$ ion (see Sec. IV B). The ^{78}Kr signal was not strong enough for spectra of sufficient quality to be recorded. The isotope shifts were found to vary linearly with the mass [0.004 02(9) cm^{-1} per mass unit], and thus the ionization potential of ^{78}Kr is predicted to lie 0.032 16(72) cm^{-1} below that of ^{86}Kr, at a position of 118 284.6813 ± 0.0190 cm^{-1}.

The average ionization energy, weighted by the relative isotopic abundances, as it would have been observed in an absorption measurement using a natural sample of krypton, is compared to earlier literature values of the $^2P_{1/2}$ ionization energy in Table VII. The present measurement is thus more accurate by a factor of more than 10 compared to earlier measurements. Table VIII summarizes the resonance parameters derived from the present measurements in a fit using Eq. (17) and compares them with results obtained in earlier studies of autoionizing resonances of Kr of lower principal quantum numbers. The agreement with the results obtained by Maeda *et al.* [19] and Klar *et al.* [24] is very good and suggests that the line profile parameters are only very weakly energy dependent [24]. The reduced resonance widths $\Gamma^*_{s'}$ and $\Gamma^*_{d'}$ obtained by Koeckhoven *et al.* [21] by (3+1) resonance-enhanced multiphoton ionization spectroscopy are larger than the results of the present study, presumably because of power broadening at the high intensities inherent to the multiphoton excitation.

MQDT calculations were also carried out using the MQDT parameters of Ref. [42], derived in the study of high Rydberg states of Kr below the $^2P_{3/2}$ ionization threshold, and the ionization energies listed in Table VI. The calculations are compared with the experimental spectra in Fig. 3. The comparison served the purposes of (1) testing the validity of the MQDT parameters of Ref. [42] in the region above the $^2P_{3/2}$ ionization threshold and (2) determining the experimental resolution. The best agreement with the experimental spectra was obtained using a ratio of the transition dipole amplitudes $D_\alpha/D_{\alpha'}=1.5$ for $\alpha=d\,^1P_1$ and $\alpha'=s\,^1P_1$.

Convolution of the spectra with a Gaussian line-shape function with a full width at half maximum of 0.007 cm^{-1} enabled the reproduction of the widths of all lines recorded

TABLE VII. Literature values of the $^2P_{1/2}$ ionization threshold of krypton in comparison with the value determined in this work.

Reference	Ionization energy $E_{i,J^+=1/2}$ (cm^{-1})[a]
Moore [12]	118284.7
Yoshino and Tanaka [15]	118284.6(2)
Kampschulte *et al.* [28]	118284.6(3)
Baig *et al.* [30]	118284.55(15)
This work	$118284.7036 \pm (0.0009)_{\mathrm{stat}} \pm (0.01)_{\mathrm{abs}}$

[a]Average value from all isotopes in a natural sample.

TABLE VIII. Comparison of the quantum defects μ_l, the asymmetry parameters q_l, and the reduced linewidths Γ_l^* determined in this work with literature values. The quantum defects were determined from a least-squares fit of the Rydberg formula, and the asymmetry parameters and reduced linewidths were deduced from a parametric fit of Eq. (17) to the experimental data. The Γ_l^* values listed for Refs. [21,19] were obtained from the linewidth parameters W_l quoted therein by use of Eq. (19).

Parameter	This work[a]	Ref. [21]	Ref. [19][b]	Ref. [24][c]
$\mu_{s'}$	3.094(1)	3.097(5) $[(n+2)=8-24]$	3.094(1)	
$\mu_{d'}$	1.243(7)	1.25(3) $(n=6-24)$	1.243(1)	
$q_{s'}$	35(4)		25.5(5.5)	34(18)
$q_{d'}$	2.3(1)		1.71(15)	
$\Gamma_{s'}^*$ (cm^{-1})	1329(18)	2096(420) $[(n+2)=8-12]$	1351(170)	1229(47)
$\Gamma_{d'}^*$ (cm^{-1})	23360(270)	32136(6990) $(n=6-20)$	29188(770)	

[a]Derived from measurements in the range $n=40-50$.
[b]Values for $14s'[2/2]_1$ and $12d'[3/2]_1$.
[c]Values for $8s'[1/2]_1$

in the measurements in which a single skimmer of orifice diameter 0.5 mm was used. The experimental resolution could be improved to 0.005 cm^{-1} by using two consecutive, 1-mm-orifice-diameter skimmers, separated by 72 mm [see Fig. 2(d)]. However, spectra of only the most abundant isotope could be measured in this configuration because of the reduction of signal intensity.

The excellent agreement between the experimental and calculated spectra of all isotopes illustrated in Fig. 3 demonstrates the ability of the MQDT parameters of Ref. [42] to describe high-resolution spectra not only in the bound region of the spectrum below the $^2P_{3/2}$ threshold, but also in the autoionization region.

B. The photoionization spectrum of ^{83}Kr

Figure 4 compares the photoionization spectra of ^{84}Kr (left-hand-side panels) and ^{83}Kr (right-hand-side panels) in

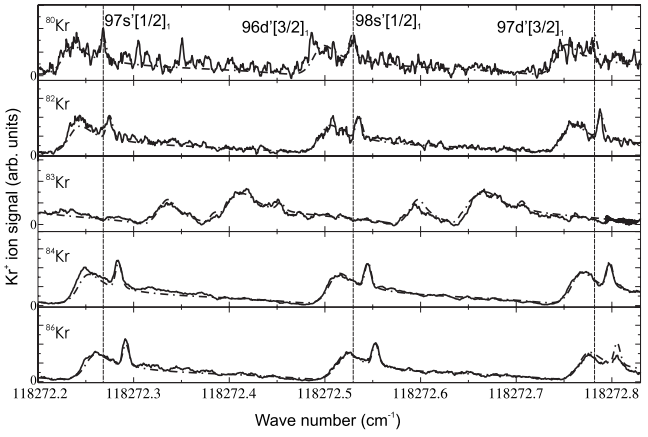

FIG. 3. Spectra of the autoionizing Rydberg states of ^{80}Kr, ^{82}Kr, ^{83}Kr, ^{84}Kr, and ^{86}Kr around $n=96$. The dash-dotted lines show the MQDT calculations which have been convoluted with a Gaussian line-shape function having a full width at half maximum of 0.007 cm^{-1}, corresponding to the experimental resolution. The dashed vertical lines indicate the spectral positions of the $97s'[1/2]_1$, $98s'[1/2]_1$, and $99s'[1/2]_1$ resonances of ^{80}Kr.

the vicinity of the $43s'$, $53s'$, and $75s'$ autoionizing resonances. The differences at $(n+2)=43$ result primarily from a splitting of the s' resonances into an $F^+=4$ and an $F^+=5$ component. The splittings of the d' resonances at these low values of n are smaller than their widths and are thus not observable. The splitting of the d' resonances becomes observable at higher n values because the width of the d' resonances decreases with $1/n^3$ [see Eq. (19)], whereas the hyperfine splitting of the $^{83}Kr^+$ $^2P_{1/2}$ level is independent of n. A low-energy d' resonance becomes observable at $n\approx 50$ and arises from $d'[5/2]_3$ and $d'[3/2]_2$ states, which gain intensity by J mixing induced by the hyperfine interaction as shown by the MQDT calculations (see below). At $n\approx 73$ the single pair of s' and d' resonances in ^{84}Kr are split in ^{83}Kr into two sets of almost equal intensity, one corresponding to the $F^+=4$, the other to the $F^+=5$ hyperfine component of the $^2P_{1/2}$ level of $^{83}Kr^+$. The photoionization spectra of ^{83}Kr and those of the $I=0$ isotopes differ significantly and, consequently, the nuclear spin plays an important role in the photoionization of Kr near threshold.

The spectra displayed in Fig. 4 were assigned on the basis of MQDT calculations carried out using the same parameters ($V_{\alpha\alpha'}$, μ_α, and D_α) as used in the analysis of the $I=0$ isotopes in the previous section. The only parameter that needed adjustment to obtain quantitatively excellent agreement with the experimental spectra was the hyperfine splitting of the $^2P_{1/2}$ state of $^{83}Kr^+$. The energetic positions $\tilde{\nu}(J^+,F^+)$ of the hyperfine components of the $(4p)^5$ $^2P_{J^+}$ $(J^+=3/2,1/2)$ states of $^{83}Kr^+$ are given by [49]

$$\tilde{\nu}(J^+,F^+)=\tilde{\nu}_{J^+}+\frac{A_{J^+}C}{2}+B_{J^+}\frac{\frac{3}{4}C(C+1)-I(I+1)J^+(J^++1)}{2I(2I-1)J^+(2J^+-1)}. \tag{20}$$

In Eq. (20), $\tilde{\nu}_{J^+}$ is the position of the barycenter of the hyperfine components and $C=F^+(F^++1)-I(I+1)-J^+(J^++1)$. A_{J^+} is the magnetic dipole hyperfine coupling constant and B_{J^+} is the electric quadrupole hyperfine coupling constant, which is zero in the case of $J^+=1/2$. Hence, the magnitude

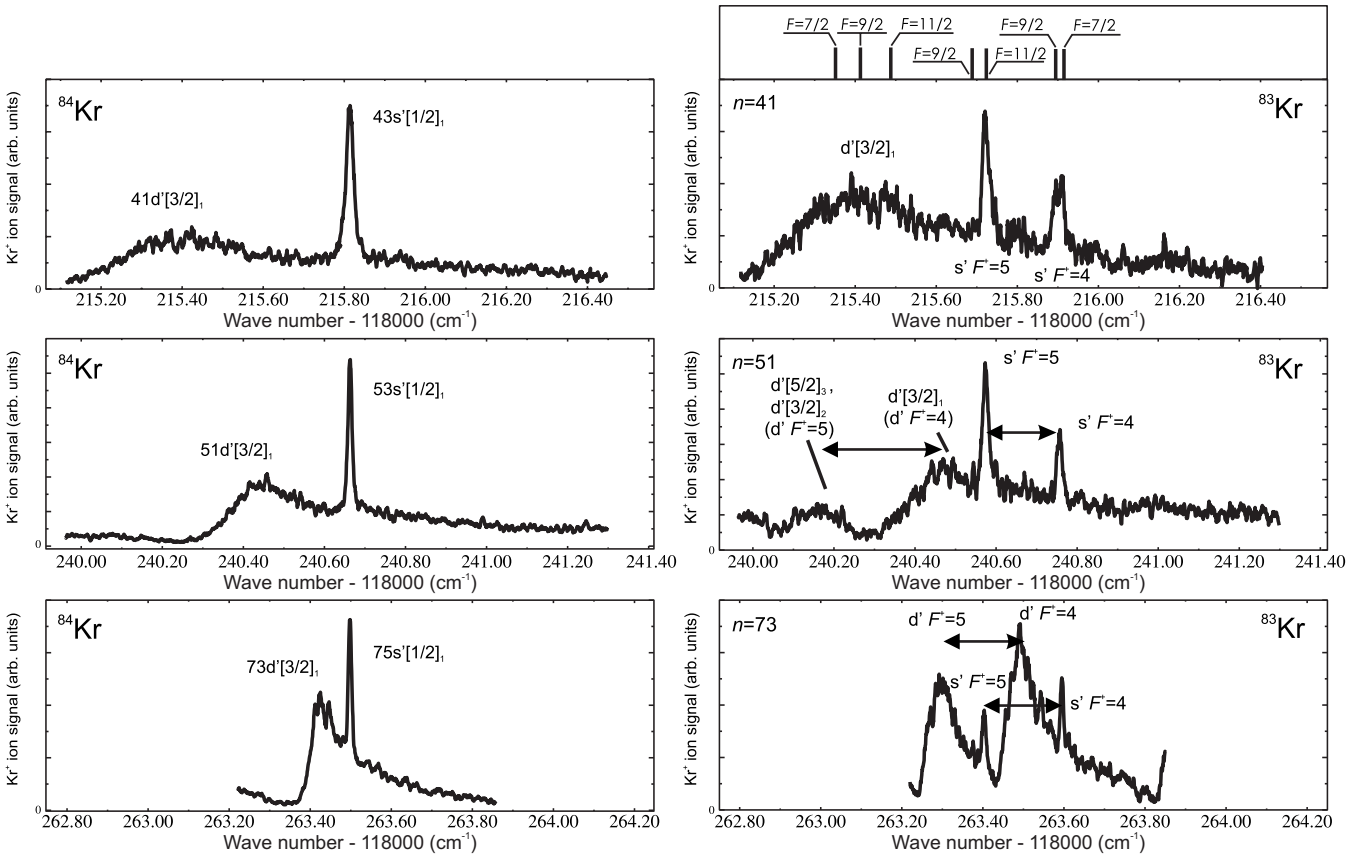

FIG. 4. Spectra of ^{84}Kr (left-hand-side panels) and ^{83}Kr (right-hand-side panels) recorded at different values of n. The splittings of the s' and d' lines of ^{83}Kr, indicated by the double-headed arrows, reflect the splitting of the ion core into $F^+=5$ and $F^+=4$ hyperfine states. With increasing n, the $J\neq 1$ d' states gain intensity through hyperfine-interaction-mediated J mixing. J mixing is already almost complete for the s' states at $n=41$ and the splitting into the $F=7/2$ and $9/2$ lines in the $F^+=4$ component is observable. The panel attached to the top of the ^{83}Kr spectrum at $n=41$ shows the positions of the resonances calculated at $n=41$ by MQDT.

of the hyperfine splitting of the $^2P_{1/2}$ state is determined only by the value of $A_{1/2}$.

The hyperfine splitting of the ion and the ionization energy of ^{83}Kr could be determined most accurately from the analysis of the spectra in the region where the sharp s' lines could still be resolved. The line positions of the s' $F^+=4,5$ components, given in Table IX, were determined by fitting the lines with Lorentzians up to $(n+2)=84$ and with Gaussians as soon as the combination of laser bandwidth and Doppler broadening became the main contribution to the linewidths. $A_{1/2}$ and $E_{i,J^+=1/2}(^{83}\mathrm{Kr})$ were then determined by extrapolating the $F^+=4$ and $F^+=5$ s' series separately using Rydberg's formula. MQDT calculations implemented in a least-squares fitting routine to determine $E_{i,J^+=1/2}(^{83}\mathrm{Kr})$ and

TABLE IX. Wave numbers of the $4p^5(n+2)s'(F^+)\leftarrow {}^1S_0(F=9/2)$ transitions of ^{83}Kr. The relative and absolute uncertainties in the line positions correspond to 0.002 and 0.013 cm^{-1}, respectively. The fourth column lists the splittings of the s' lines into the two hyperfine components $F^+=4$ and $F^+=5$. These values were obtained directly from the measured spectra.

$(n+2)$	$\tilde{\nu}(F^+=5)$ (cm^{-1})	$\tilde{\nu}(F^+=4)$ (cm^{-1})	Main hyperfine splitting of the $s'[1/2]_1$ series (cm^{-1})
43	118215.7200	118215.9001	0.1802(13)
48	118230.2041	118230.3908	0.1854(22)
53	118240.5739	118240.7565	0.1819(14)
75	118263.4035	118263.5961	0.1925(11)
84	118267.8639	118268.0556	0.1921(11)
98	118272.4354		
100	118272.9347		
102	118273.4012		

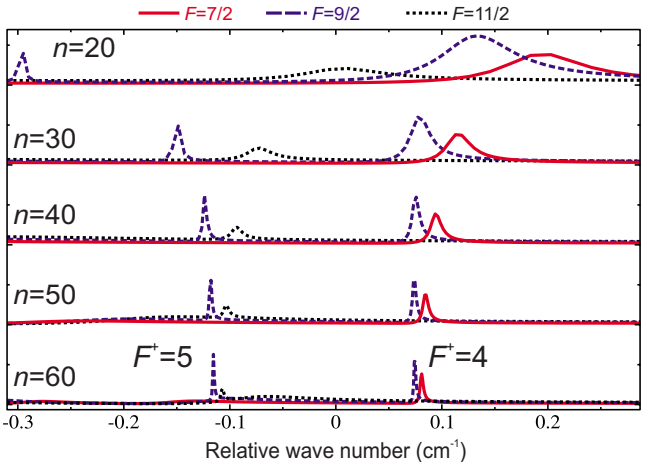

FIG. 5. (Color online) MQDT calculations carried out at different values of n, showing the different evolutions of the s' F states, presented on a relative wave number scale with zero at the position of the barycenter of the hyperfine structure. As n increases, the $F=9/2$ line located on the left-hand side of the spectrum at $n=20$ gains intensity from hyperfine-mediated J mixing of the $s'[1/2]_0$ state with the $s'[1/2]_1$ and eventually groups together with the $F=11/2$ component, forming the $F^+=5$ hyperfine component of the s' lines when J mixing is complete at $n=60$.

$A_{1/2}$ were also carried out for the $F^+=4$ and $F^+=5$ states. In this fitting procedure, $E_{i,J^+=1/2}(^{83}\mathrm{Kr})$ and $A_{1/2}$ were iteratively adjusted until the differences between the s' $F^+=4,5$ line centers of the calculated and the experimental spectra were minimized. The values for $E_{i,J^+=1/2}(^{83}\mathrm{Kr})$ obtained with both methods agreed within their uncertainties and a weighted average was taken for the final result given in Table VI. The two results for $A_{1/2}$ were also in agreement, but a more precise value was obtained by running iterative MQDT calculations in which solely $A_{1/2}$ was fitted until the differences in the $F^+=4-F^+=5$ hyperfine intervals in the simulated spectra and those in the experimental spectra were minimized. This procedure had the advantage that the contributions of the absolute wave-number uncertainties in the line positions were eliminated. $A_{1/2}$ was determined to be $-0.0385(5)$ cm^{-1}, implying a hyperfine splitting of the $^2P_{1/2}$ ionic state of $0.1925(25)$ cm^{-1}, close to the prediction of 0.2 cm^{-1} made in Ref. [41].

Figure 5 shows a MQDT calculation of the spectra of the s' states at different values of n, plotted on a relative wave-number scale with zero at the barycenter of the hyperfine structure. F components arising from coupling of $\vec{j}$ with $\vec{F}^+$ evolve differently as n increases: At $n=20$, three peaks make up the typical sharp $s'[1/2]_1$ line of the spectra, and a fourth sharper but weaker line, attributed to the $s'[1/2]_0$ state, becomes observable on the left-hand side of the figure. The $F=11/2$ state moves to the red relative to the $F=9/2$ and $7/2$ states and joins the $s'[1/2]_0$ to form the two components associated with the $F^+=5$ hyperfine level of the ion. The $F=9/2$ and $7/2$ components remain approximately at the same position and form the two components of the $F^+=4$ manifold. Comparison of the calculations presented in Fig. 5 with the measured intervals between the $F^+=4$ and $F^+=5$ components of the $s'[1/2]_1$ levels enables one to interpret the slight increase in the observed splitting of the s' levels at low n values (see Table IX) as arising from the splitting between the $F=11/2$ component of the $F^+=5$ and the $F=7/2$ and $9/2$ components of the $F^+=4$ level.

When the hyperfine splitting $\Delta E_{F^+=5,F^+=4}$ becomes equal to the separation between Rydberg states of principal quantum number n and $n+m$, $\Delta E_{n,n+m} \cong m\Delta E_{n,n+1}$, the hyperfine structure vanishes, leading to the appearance of "strobo-

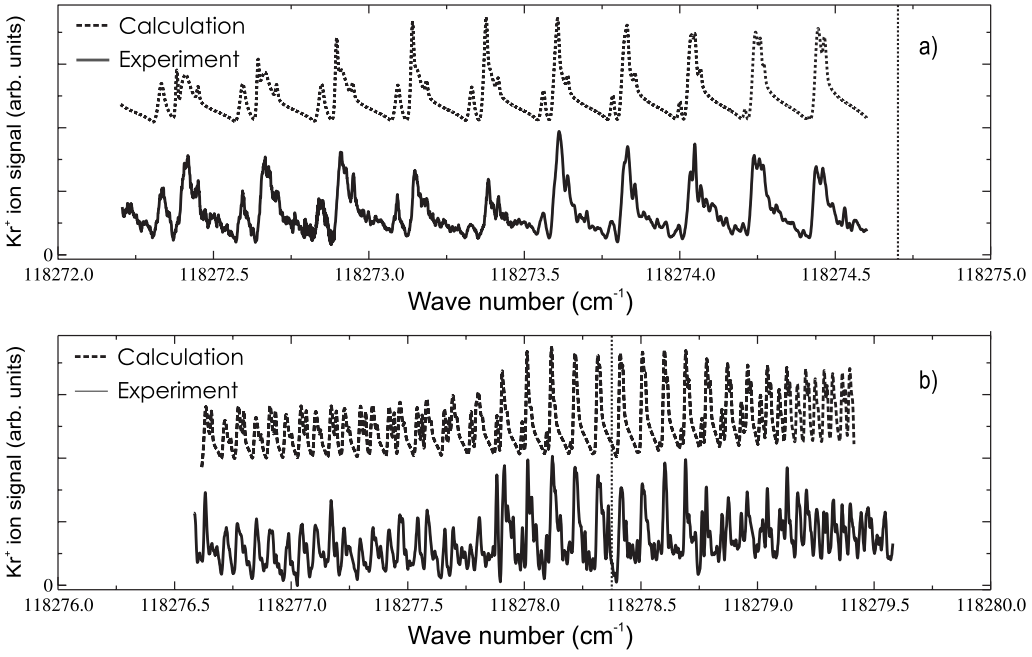

FIG. 6. Stroboscopic resonances in ^{83}Kr around (a) $n=106$ and (b) $n=133$. When the orbital period of the Rydberg electron becomes equal to the period of precession of the ion core spins, the hyperfine structure vanishes. The vertical dashed lines at $\sim$118 274.7 cm^{-1} in (a) and at $\sim$118 278.4 cm^{-1} in (b) indicate these positions.

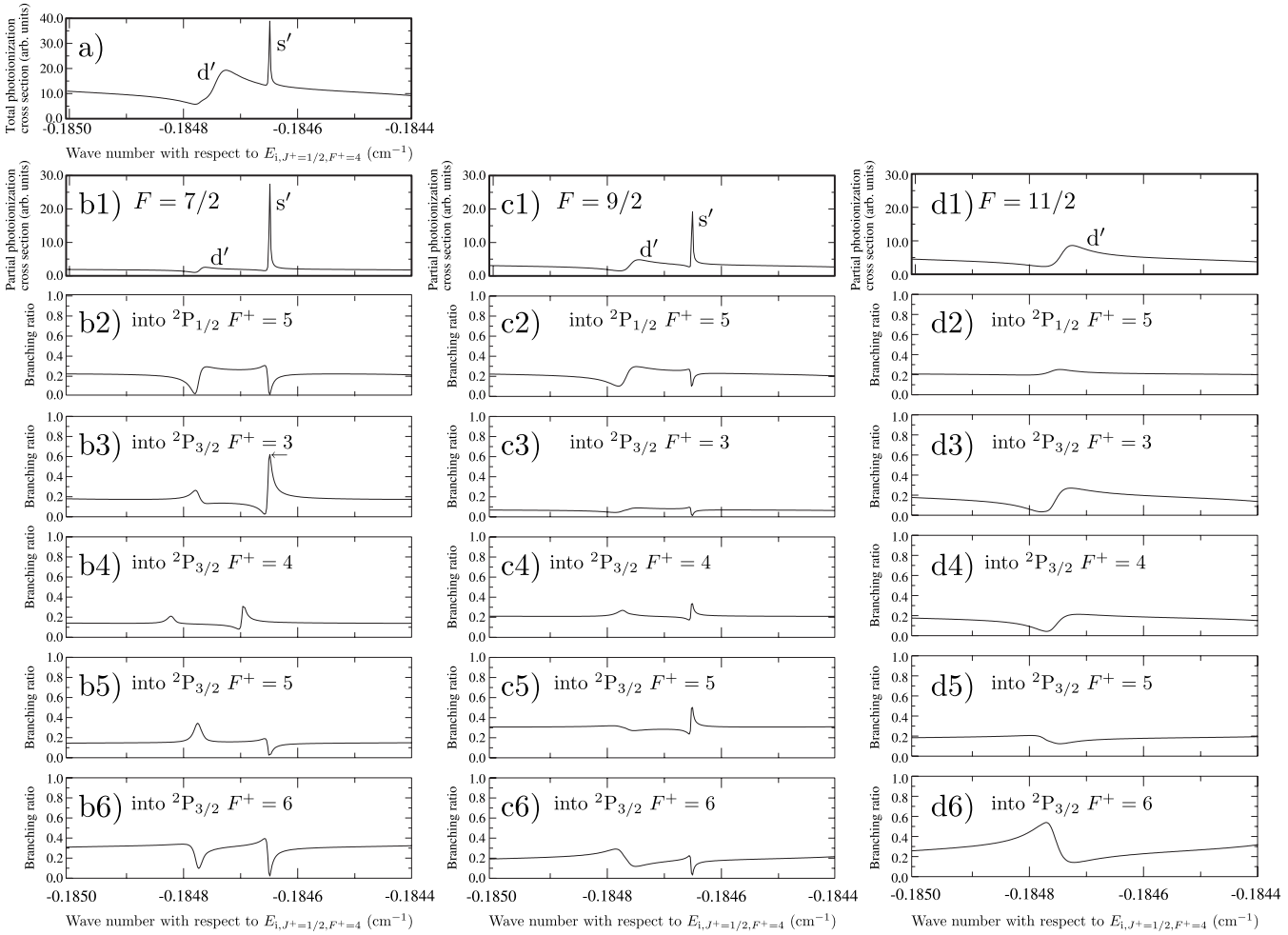

FIG. 7. Total and partial photoionization cross sections between the $F^+=5$ and $F^+=4$ hyperfine levels of the $^2P_{1/2}$ state of $^{83}Kr^+$. In (a) the total photoionization cross section of ^{83}Kr is shown. (b1), (c1), and (d1) show the partial photoionization cross sections of the $F=7/2$, $9/2$, and $11/2$ channels, respectively. (b2)–(b6), (c2)–(c6), and (d2)–(d6) show the branching ratios of the respective channels into the ionization continua associated with the hyperfine levels of $^{83}Kr^+$, i.e., $^2P_{1/2}$ $F^+=5$, $^2P_{3/2}$ $F^+=6$, 5, 4, and 3.

scopic" resonances, as observed in the spectra of ^{129}Xe and ^{131}Xe [31]. In ^{83}Kr, the first stroboscopic resonance ($m=1$) occurs around the $106d'$ resonance, where the period of the Rydberg electron equals the period of precession of the ion core spins. The spectrum in the vicinity of this point is shown in Fig. 6(a) where the upper, dashed trace shows a MQDT calculation using the hyperfine splitting and the ionization energy determined from the analysis of the experimental spectra. Around $n=133$, the next, $m=2$, stroboscopic resonance is encountered and is shown in Fig. 6(b). The accuracy of the value of $A_{1/2}$ could be checked by the reproduction, in the MQDT calculations, of the positions of the observed stroboscopic resonances, which are very sensitive to the value of $A_{1/2}$. Beyond the $m=1$ stroboscopic resonance, the period of the electronic motion exceeds the period associated with the hyperfine interaction in the ion core, which implies that the time scale of the electronic motion is slower than that of the precession of the spins in the $^{83}Kr^+$ core. This situation represents a rather unusual hierarchy of time scales.

The excellent agreement between the experimental and calculated photoionization spectra of ^{83}Kr in the vicinity of the stroboscopic resonances confirms that the MQDT parameters on which these calculations rely are of sufficient accuracy to explore aspects of the photoionization dynamics that are not directly accessible in the experiments presented here. These aspects are discussed in the next section.

C. Partial photoionization cross sections: The role of the nuclear spin

Autoionizing Rydberg states converging to the $F^+=4$ upper hyperfine component of the $^2P_{1/2}$ state located between the $F^+=5$ and $F^+=4$ components of the $^2P_{1/2}$ ionization threshold (see Fig. 1) can autoionize either into the $J^+=1/2$, $F^+=5$ continuum by transfer of hyperfine energy from the core to the Rydberg electron (a process designated "hyperfine autoionization" [31]) or by spin-orbit autoionization into one or more of the four continua associated with the $^2P_{3/2}$ ionic state. To investigate whether hyperfine and spin-orbit autoionization differ in their rates, the partial cross sections $\sigma_{J^+F^+}$ [see Eq. (15)] for autoionization into all open channels ($J^+=1/2$, $F^+=4$, and $J^+=3/2$, $F^+=3-6$) have been calculated with the optimal MQDT parameters.

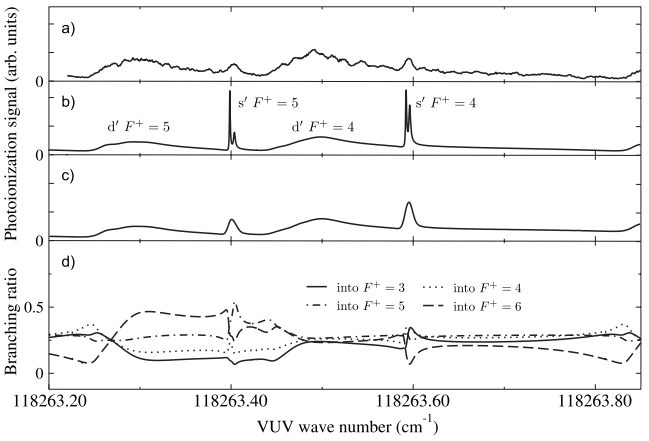

FIG. 8. Branching ratios of the autoionizing states of ^{83}Kr at $n=73$. The trace in (a) corresponds to the experimental spectrum, that in (b) to the calculated spectrum, and that in (c) shows the result of convoluting the calculated spectrum with a Gaussian profile of full width at half maximum of 0.007 cm^{-1}, corresponding to the experimental resolution. (d) shows the branching ratios into the continua associated with the $F^+=3$, 4, 5, and 6 hyperfine levels of $^2P_{3/2}$ ^{83}Kr$^+$.

Because the total angular momentum $\vec{F}$ is a constant of motion and does not change upon ionization, separate calculations were performed for $F=7/2$, $9/2$, and $11/2$. For each F value, the branching ratios $\sigma_{J^+F^+}/\sigma_{\mathrm{tot}}$ into each open channel were then determined over an energy range corresponding to one unit of the effective principal quantum number ($n^*=775-776$) of the autoionizing series. The results are displayed in Fig. 7, where panel (a) shows the total photoionization cross section and panels (b1), (c1), and (d1) show the contributions to the total photoionization cross section from channels with $F=7/2$, $9/2$, and $11/2$, respectively. Figures 7(b2)–7(b6), 7(c2)–7(c6), and 7(d2)–7(d6) give, in each case, the branching ratio into the five open channels indicated above each trace. Only d components contribute to the $F=11/2$ channels whereas the $F=7/2$ and $9/2$ channels consist of both s and d contributions. The following overall behavior can be diagnosed from Fig. 7.

(1) The total photoionization cross section in this region shows resonances characterized by the same Beutler-Fano profiles as the $I=0$ isotopes between the $^2P_{3/2}$ and $^2P_{1/2}$ thresholds. The reduced widths of these resonances correspond almost exactly to those determined for the $I=0$ isotopes.

(2) The overall contribution to the total photoionization cross section increases in the sequence $F=7/2$, $9/2$ and $11/2$ [compare Figs. 7(b1), 7(c1), and 7(d1)]. This behavior parallels the increase of the $2F+1$ multiplicity of the channels.

(3) Within each set of calculations performed for a given F value, the branching ratios in the region far from the resonances all lie close to the statistical values of 0.2. This observation suggests that hyperfine and spin-orbit autoionization have similar rates, an observation that supports the conclusion drawn in Ref. [31] that spin-orbit and hyperfine autoionization have their origin in the same interactions between the core and Rydberg electrons (see Ref. [31] for additional discussion).

(4) Appreciable deviations of the branching ratios from the statistical values occur in the vicinity of the centers of the autoionizing resonances. This effect is particularly pronounced for the s' resonance in the $F=7/2$ channels. At the position of the arrow in Fig. 7(b3), the $J^+=3/2$, $F^+=3$ channel represents more than 60% of the $F=7/2$ contribution to the total photoionization cross section, whereas the ionization into $J^+=1/2$, $F^+=5$, the $J^+=3/2$, $F^+=5$, and $J^+=3/2$, $F^+=6$ channels is strongly suppressed. Selective excitation to the s' $F=7/2$ resonances may thus be exploited to produce state-selected hyperfine levels of ^{83}Kr$^+$. Similarly, the $J^+=3/2$, $F^+=6$ channel is favored at the position of the d' resonance of $F=11/2$ [see Figs. 7(d1)–7(d6)].

Figure 8 shows the experimental [panel (a)] and calculated [panels (b) and (c)] photoionization cross sections in the region between the $^2P_{3/2}$ and $^2P_{1/2}$ thresholds at a total excitation wave number of 118 263.6 cm^{-1} corresponding to $n=73$ Rydberg states converging to the $^2P_{1/2}$ $F^+=4$ and 5 thresholds. Figure 8(c) represents a convolution of the MQDT prediction in Fig. 8(b) with a Gaussian line-shape function of full width at half maximum of 0.007 cm^{-1}, and reproduces the experimental spectrum well.

Figure 8(d) provides an overview of the branching ratios into the four open channels associated with the $^2P_{3/2}$ ground state. Here again, the branching ratios lie close to the statistical value of 0.25 with significant deviations near the centers of the resonances. For example, the $F^+=6$ channels are suppressed at ~118 263.24, ~118 263.59, and ~118 263.82 cm^{-1}, but enhanced from ~118 263.30 to ~118 263.40 cm^{-1}.

The experimental observation of pure hyperfine autoionization would represent an important milestone in Rydberg state spectroscopy and in the study of photoionization dynamics. A MQDT prediction of pure hyperfine autoionization

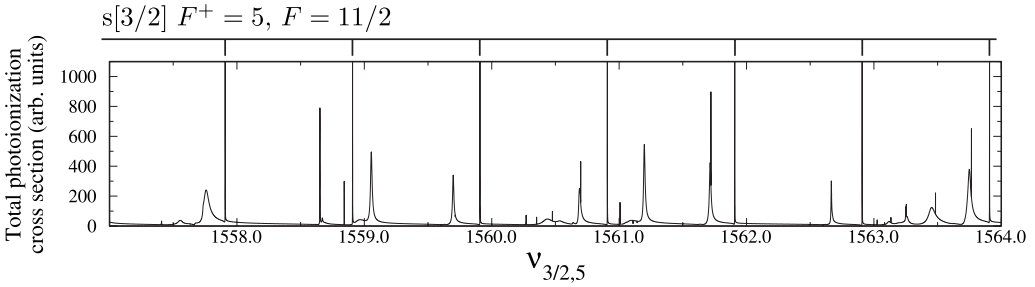

FIG. 9. Total photoionization cross section, calculated by MQDT, between the $F^+=5$ and 6 hyperfine levels of ^{83}Kr$^+$ ($^2P_{3/2}$), plotted on a scale corresponding to the effective principal quantum number $\nu_{J^+=3/2,F^+=5}$.

in ^{83}Kr is displayed in Fig. 9. The figure shows a calculation of the total photoionization cross section in a narrow range of energies corresponding to effective principal quantum numbers between 1557 and 1564 below the $J^+=3/2$, $F^+=5$ first excited hyperfine level of $^{83}Kr^+$. In this region, s and d Rydberg states belonging to series converging on the higher-lying hyperfine levels of $^{83}Kr^+$ ($J^+=3/2$, $F^+=5$, 4, and 3) overlap. The calculation predicts many autoionizing resonances of very different widths, shapes, and intensities. All resonances in the figure correspond to Rydberg states that decay by hyperfine autoionization. The predicted spectral patterns are so complex that only one series, the $ns[3/2]$ $F^+=5$, $F=11/2$ series, can be unambiguously identified (see assignment bar). The widths of these sharp resonances ($\Gamma=1.7\times10^{-8}$ cm^{-1} at $n=1557$) can be analyzed using Eq. (19) and correspond to a reduced width of $\Gamma^*\cong60$ cm^{-1} which is much less than the value of $\Gamma^*=1329$ cm^{-1} for the s' resonances of the $I=0$ isotopes. Other resonances in the figure have widths more than two orders of magnitude larger. The dynamics of autoionization is thus predicted to be unusually complex.

V. CONCLUSIONS

The results presented in this paper provide a complete survey of the isotope effects in the photionization of Kr. The photoionization spectra of the $I=0$ isotopes differ only by a constant energy shift of 0.004 02(9) cm^{-1}/u. The $^2P_{1/2}$ ionization energy of Kr could be measured with a more than tenfold increase in accuracy compared to previous measurements and isotope selectively. The experimental results and the MQDT predictions illustrate that the nuclear spin in ^{83}Kr ($I=9/2$) leads to a wealth of spectral structures and related competing dynamical processes that are absent in the $I=0$ isotopes. The preferential production of certain hyperfine levels at selected wave numbers provides a method to prepare Kr^+ ions in selected hyperfine levels, with possible applications in the study of ion-molecule reactions.

The considerable differences observed here between the photoionization spectra of ^{83}Kr and those of the $I=0$ isotopes, both in terms of spectral structures and in terms of the underlying autoionization processes, combined with similar observations made in Xe and H_2, imply that the widespread view that the nuclear spins can be disregarded in the treatment of atomic and molecular photoionization spectra must be revised.

ACKNOWLEDGMENTS

We thank Dr. M. Schäfer (ETH Zurich) and Prof. H. Hotop (TU Kaiserslautern) for useful discussions and suggestions and Dr. H. J. Wörner for his help with the MQDT calculations. This work was supported financially by the Swiss National Science Foundation under Project No. 200020-116245.

[1] H. Beutler, Z. Phys. **93**, 177 (1935).
[2] U. Fano, Phys. Rev. **124**, 1866 (1961).
[3] K. T. Lu, Phys. Rev. A **4**, 579 (1971).
[4] M. J. Seaton, Proc. Phys. Soc. London **88**, 801 (1966).
[5] K. T. Lu and U. Fano, Phys. Rev. A **2**, 81 (1970).
[6] C.-M. Lee and K. T. Lu, Phys. Rev. A **8**, 1241 (1973).
[7] U. Fano, J. Opt. Soc. Am. **65**, 979 (1975).
[8] H. H. Fielding and T. P. Softley, J. Phys. B **25**, 4125 (1992).
[9] U. Fano, Phys. Rev. A **2**, 353 (1970); **15**, 817(E) (1977).
[10] C. H. Greene and Ch. Jungen, Adv. At. Mol. Phys. **21**, 51 (1985).
[11] *Molecular Applications of Quantum Defect Theory*, edited by Ch. Jungen (Institute of Physics Publishing, Bristol, 1996).
[12] C. E. Moore, *Atomic Energy Levels*, Natl. Bur. Stand. (U.S.). Circ. No. 467/2 (U.S. GPO, Washington, DC, 1952).
[13] J. Sugar and A. Musgrove, J. Phys. Chem. Ref. Data **20**, 859 (1991).
[14] E. B. Saloman, J. Phys. Chem. Ref. Data **36**, 215 (2007).
[15] K. Yoshino and Y. Tanaka, J. Opt. Soc. Am. **69**, 159 (1979).
[16] J. Z. Wu, S. B. Whitfield, C. D. Caldwell, M. O. Krause, P. van der Meulen, and A. Fahlman, Phys. Rev. A **42**, 1350 (1990).
[17] K. Ueda, K. Maeda, K. Ito, and T. Namioka, J. Phys. B **22**, L481 (1989).
[18] K. Maeda, K. Ueda, K. Ito, and T. Namioka, Phys. Scr. **41**, 464 (1990).
[19] K. Maeda, K. Ueda, and K. Ito, J. Phys. B **26**, 1541 (1993).
[20] J. L. Dehmer, S. T. Pratt, and P. M. Dehmer, Phys. Rev. A **36**, 4494 (1987).
[21] S. M. Koeckhoven, W. J. Buma, and C. A. de Lange, Phys. Rev. A **49**, 3322 (1994).
[22] M. Ahmed, M. A. Zia, M. A. Baig, and B. Suleman, J. Phys. B **30**, 2155 (1997).
[23] D. Klar, M. Aslam, M. A. Baig, K. Ueda, M.-W. Ruf, and H. Hotop, J. Phys. B **34**, 1549 (2001).
[24] D. Klar, K. Harth, J. Ganz, T. Kraft, M.-W. Ruf, H. Hotop, V. Tsemekhman, K. Tsemekhman, and M. Ya. Amusia, Z. Phys. D: At., Mol. Clusters **23**, 101 (1992).
[25] I. D. Petrov, V. L. Sukhorukov, and H. Hotop, J. Phys. B **35**, 323 (2002).
[26] T. Peters, T. Halfmann, U. Even, A. Wünnenberg, I. D. Petrov, V. L. Sukhorukov, and H. Hotop, J. Phys. B **38**, S51 (2005).
[27] C. Delsart and J.-C. Keller, Phys. Rev. A **28**, 845 (1983).
[28] T. Kampschulte, J. Schulze, D. Luggenhölscher, M. D. Bowden, and U. Czarnetzki, New J. Phys. **9**, 18 (2007).
[29] A. Wada and C. Hirose, J. Mol. Struct. **379**, 205 (1996).
[30] M. A. Baig and M. Aslam, J. Phys. B **41**, 035004 (2008).
[31] H. J. Wörner, M. Grütter, E. Vliegen, and F. Merkt, Phys. Rev. A **71**, 052504 (2005), **73**, 059904(E) (2006).
[32] H. J. Wörner, S. Mollet, Ch. Jungen, and F. Merkt, Phys. Rev. A **75**, 062511 (2007).
[33] R. Seiler, Th. A. Paul, M. Andrist, and F. Merkt, Rev. Sci. Instrum. **76**, 103103 (2005).
[34] Th. A. Paul and F. Merkt, J. Phys. B **38**, 4145 (2005).
[35] F. Brandi, W. Hogervorst, and W. Ubachs, J. Phys. B **35**, 1071

(2002).

[36] S. Gerstenkorn, J. Vergès, and J. Chevillard, *Atlas du Spectre d'Absorption de la Molécule d'Iode:* 11 000–14 000 cm^{-1} (Laboratoire Aimé-Cotton CNRS II, Orsay, France, 1982); see correction in [50].

[37] The Doppler-free reference measurement of the $a1$, $a2$, and $a3$ hyperfine components of the $R(107)$ line of the $B\,^3\Pi_u^+ - X\,^1\Sigma_g^+$ (20-1) band listed as No. 2075 at 11 761.6379 cm^{-1} in the iodine atlas [36] at 352 604 382.14, 352 604 399.73, and 352 604 417.55 GHz, respectively, with an uncertainty of 500 kHz, was kindly provided by W. Ubachs and co-workers at the Department of Physics and Astronomy of the Vrije Universiteit Amsterdam, The Netherlands.

[38] Th. A. Paul, H. A. Cruse, H. J. Wörner, and F. Merkt, Mol. Phys. **105**, 871 (2007).

[39] Ch. Jungen and O. Atabek, J. Chem. Phys. **66**, 5584 (1977).

[40] M. Aymar, O. Robaux, and C. Thomas, J. Phys. B **14**, 4255 (1981).

[41] H. J. Wörner, U. Hollenstein, and F. Merkt, Phys. Rev. A **68**, 032510 (2003).

[42] M. Schäfer and F. Merkt, Phys. Rev. A **74**, 062506 (2006).

[43] R. N. Zare, *Angular Momentum* (John Wiley & Sons, New York, 1988).

[44] C. M. Lee, Phys. Rev. A **10**, 1598 (1974).

[45] E. U. Condon and G. H. Shortley, *The Theory of Atomic Spectra* (Cambridge University Press, Cambridge, U.K., 1953).

[46] U. Fano and J. W. Cooper, Phys. Rev. **137**, A1364 (1965).

[47] M. J. Seaton, Rep. Prog. Phys. **46**, 167 (1983).

[48] K. Ueda, Phys. Rev. A **35**, 2484 (1987).

[49] H. Kopfermann, *Nuclear Moments* (Academic Press, San Diego, 1958).

[50] S. Gerstenkorn and P. Luc, Rev. Phys. Appl. **14**, 791 (1979).